

# Impact of Cloud Microphysical Processes on the Simulation of Typhoon Ranim near Shore. Part II: Typhoon Intensity and Track\*

CHENG Rui<sup>1,2†</sup>(程 锐), YU Rucong<sup>1</sup>(宇如聪), XU Youping<sup>1,2</sup>(徐幼平), and FU Yunfei<sup>3</sup>(傅云飞)

<sup>1</sup> State Key Laboratory of Numerical Simulation for Atmospheric Sciences and Geophysical Fluid Dynamics, Institute of Atmospheric Physics, CAS, Beijing 100029

<sup>2</sup> Graduate School of the Chinese Academy of Sciences, Beijing 100049

<sup>3</sup> University of Science and Technology of China, Hefei 230026

(Received August 11, 2010)

## ABSTRACT

The impact of cloud microphysical processes on the simulated intensity and track of Typhoon Ranim is discussed and analyzed in the second part of this study. The results indicate that when the cooling effect due to evaporation of rain water is excluded, the simulated 36-h maximum surface wind speed of Typhoon Ranim is about  $7 \text{ m s}^{-1}$  greater than that from all other experiments; however, the typhoon landfall location has the biggest bias of about 150 km against the control experiment. The simulated strong outer rainbands and the vertical shear of the environmental flow are unfavorable for the deepening and maintenance of the typhoon and result in its intensity loss near the landfall. It is the cloud microphysical processes that strengthen and create the outer spiral rainbands, which then increase the local convergence away from the typhoon center and prevent more moisture and energy transport to the inner core of the typhoon. The developed outer rainbands are supposed to bring dry and cold air mass from the middle troposphere to the planetary boundary layer (PBL). The other branch of the cold airflow comes from the evaporation of rain water itself in the PBL while the droplets are falling. Thus, the cut-off of the warm and moist air to the inner core and the invasion of cold and dry air to the eyewall region are expected to bring about the intensity reduction of the modeled typhoon. Therefore, the deepening and maintenance of Typhoon Ranim during its landing are better simulated through the reduction of these two kinds of model errors.

**Key words:** typhoon intensity, cloud microphysical processes, spiral rainband, environmental wind shear

**Citation:** Cheng Rui, Yu Rucong, Xu Youping, et al., 2011: Impact of cloud microphysical processes on the simulation of Typhoon Ranim near shore. Part II: Typhoon intensity and track. *Acta Meteor. Sinica*, **25**(4), 456–466, doi: 10.1007/s13351-011-0406-z.

## 1. Introduction

In this paper, we will discuss the influence of cloud microphysics on the intensity and track of a typhoon, using the experimental schemes presented in a companion paper (Part I, this issue). On the one hand, the intensity of a typhoon can be changed through environmental impacts of the large-scale circulation, vertical wind shear, sea surface temperature (SST), land surface characteristics and topography, etc. It is well known that the cutting off of water vapor transport, strong vertical wind shear, low SST, and rough under-

lying surface are unfavorable for the typhoon development (Li et al., 2004; Chen et al., 2004). On the other hand, the intensity of a typhoon can be affected by the typhoon structure as well. However, the influence of internal structure of the typhoon on its intensity is too complicated.

In recent years, some studies about the impact of evolution of outer spiral rainbands on the typhoon strength have been performed based on the analysis of cloud microphysical features. Basically, the spiral rainbands are favorable for the typhoon strengthening during the early stage of its development since they

\*Supported by the National Basic Research and Development (973) Program of China (2004CB418304).

†Corresponding author: c4rui@mail.iap.ac.cn.

(Chinese version published in Vol. 67, No. 5, 777–786, 2009)

©The Chinese Meteorological Society and Springer-Verlag Berlin Heidelberg 2011

can provide the eyewall with energy and water. Nevertheless, they can prevent the typhoon from deepening during its mature stage. Barnes et al. (1983) pointed out that convective-scale updrafts and downdrafts presented in the spiral rainbands are responsible for the thermodynamic modification of the cloud and sub cloud layers. A decrease of 12 K in equivalent potential temperature was observed when the air parcel was transported radially in the sub cloud layers. They also found that the spiral rainbands could be a barrier to the inflow. Powell (1990) revealed that the convective downdrafts could bring the cold and dry air parcels with low equivalent potential temperature to the surface. If those parcels with low equivalent potential temperature were advected to the convection-active area near the inner core of a tropical cyclone (TC), the intensity of the TC would be reduced. Wang (2002) reported that active spiral rainbands and associated strong downdrafts were unfavorable for the typhoon intensification. The formation and maintenance of spiral rainbands and downdrafts were affected by the melting of snow and graupel, the evaporation of rain water (mainly below the freezing level), and the cooling effect due to the sublimation of ice-phase particles detrained from the cloud (especially in the upper troposphere), which could limit the intensification and final strength of the TC.

Although the downdrafts could also be generated by the eyewall convection, their effect was not so important as those in the spiral rainbands, especially after the TC reached certain intensity and it was both warm and moist in the eyewall. However, Zhu and Zhang (2006) demonstrated that the cooling due to the melting was most pronounced in the eyewall region where more frozen hydrometeors especially graupel were available, whereas the evaporative cooling appeared more markedly when the TCs' environment was more unsaturated. Also, the cooling effect of evaporation on the typhoon was similar to that of the melting, but the former was present at the lower levels and the latter occurred just below the melting level.

It can be seen that typhoon intensity is quite sensitive to cloud microphysical details. This, however, has some uncertainty so far and needs to be studied

further. In this paper, sensitivity analysis is conducted to discuss the influence of varying cloud microphysical processes on the intensity and track of typhoon Rananim, and the reason why the simulated typhoon intensity is reduced near its landfall is probed.

## 2. Impact of the cloud microphysical processes on typhoon strength and track

Model configuration and experimental design are described in Part I of this paper. Please refer to Table 1 of Part I for experimental details.

### 2.1 Influence on the typhoon intensity

It can be seen from Fig. 1 that the evolutionary feature of surface maximum wind speeds in various sensitivity experiments agrees generally well with that in the control experiment. For instance, the deepening of Typhoon Rananim during 9–24 h is depicted by all the schemes, among which the biggest bias of the maximum wind speed between CTRL and the observation approaches  $5 \text{ m s}^{-1}$ . We can still see that the simulated intensities in all experiments are notably underestimated after 30 h, which is different from the fact that the real TC keeps certain intensity during that period. Section 3 will explain why the model intensity of the typhoon is markedly reduced near its landfall. It should also be noticed that the intensity of Rananim from the Japan mesoscale reanalysis data has a pronounced departure from the reality 6 h before the landfall. It seems that the maintenance of Rananim's intensity is yet difficult for us to well understand and simulate as it approaches the land.

The final intensity of the simulated typhoon in experiment NEVP is the closest to the observation, and the surface maximum wind speed is over  $7 \text{ m s}^{-1}$  greater than that in all other experiments. It is revealed (Fig. 11c in Part I) that the planetary boundary layer (PBL) outside the eyewall has high temperatures when the cooling effect due to the evaporation of rain water is excluded. This is not only because the downdrafts are reduced and confined to the narrow area beyond the eyewall (see Fig. 4a in Part I, with the peak value of  $0.5 \text{ Pa s}^{-1}$ ), but also because the subsidence mainly occurs close to the freezing level or

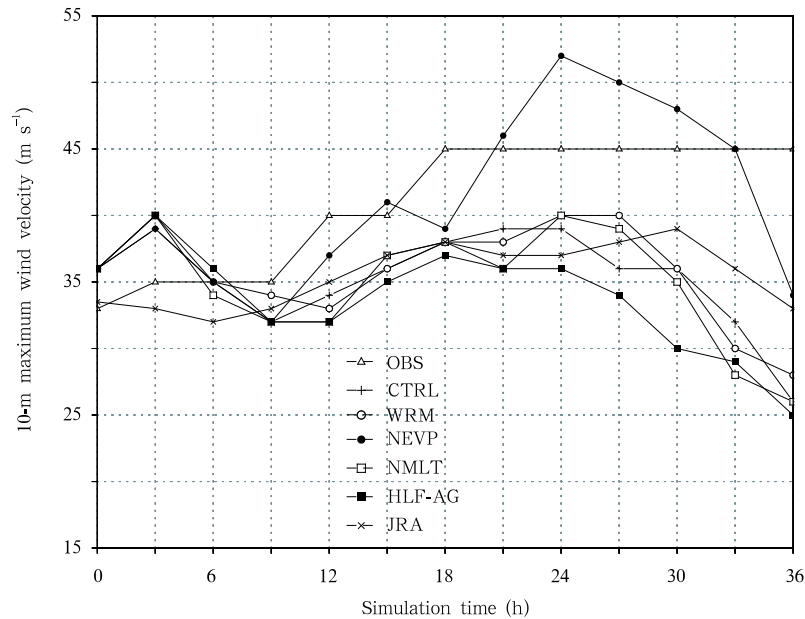


**Fig. 1.** Time series of surface maximum wind speed ( $\text{m s}^{-1}$ ) from the observation and the model simulations. OBS, CTRL, WRM, NEVP, NMLT, HLF-AG, and JRA respectively represent observation, control experiment, warm cloud experiment, experiment with cooling due to evaporation of rain water excluded, experiment with melting of snow and graupel excluded, experiment with terminal velocity of graupel made half, and the mesoscale reanalysis of Japan. The same conventions for experiment names are used hereinafter.

in the PBL and few cold and dry air parcels entrain from middle levels to the PBL. Obviously, the typhoon simulated by NEVP has a fast intensification and a strong final intensity since less cold and dry airflow invades into the eyewall. Nevertheless, NEVP overestimates the typhoon intensity during 21–33 h with the biggest departure of above  $5 \text{ m s}^{-1}$  from the observation. This is similar to the simulation of Wang (2002) and Pattnaik and Krishnamurti (2007), who pointed out that the modeled tropical cyclone was remarkably strengthened when the evaporation of rain water and the melting of snow and graupel were not considered or the melting of ice, snow and graupel was excluded.

Generally, the typhoons simulated by experiments WRM and NMLT are somewhat stronger than or close to the one from CTRL, which results from the fact that the cooling in the middle and lower troposphere is reduced and then cold and dry invasion into the inner core is weakened as well. Nevertheless, HLF-AG simulates a weaker typhoon than CTRL. When the terminal velocity is reduced by half, the downward flux of graupel is reduced so that the hydrometeor content

is decreased in the eyewall but increased in the outer rainbands. After graupel falls across the freezing level, the melting occurs and then the evaporation happens, which can result in strong cooling and downdrafts in the outer rainbands. Hence, the typhoon development will be prohibited if the adiabatic warming due to the subsidence cannot offset the cooling effect as above.

The evolution of the central sea level pressure of Ranim (figure omitted) also shows the deepening of the model typhoon during the first 24 hours, but afterwards, the typhoon intensity is reduced dominantly, especially during the 6 h before landing.

## 2.2 Influence on the typhoon track

Figure 2a shows that the model track in CTRL is the closest to the reality, and experiments WRM and NMLT produce faster traveling speeds of the typhoon before its landing. The track in HLF-AG deflects clockwise from that in CTRL. NEVP, however, has a counterclockwise deflection from CTRL, and the deviation becomes gradually visible after 24 h. At 1200 UTC 12 August, NEVP shows the largest departure

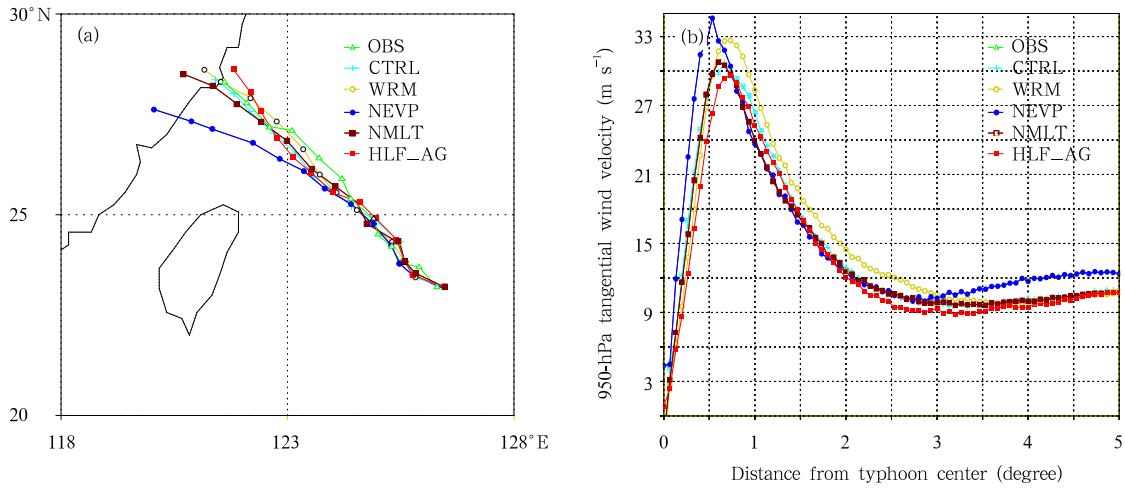


**Fig. 2.** (a) The observed and simulated typhoon tracks, and (b) profiles of the 6-h mean, azimuthally averaged tangential wind velocity ( $\text{m s}^{-1}$ ) at 950 hPa averaged between 24 and 30 h simulation time.

of about 200 km from the observation. Figure 2b describes profiles of 6-h mean, azimuthally averaged tangential wind velocity at 950 hPa. It can be seen that NEVP produces the strongest tangential winds whereas HLF\_AG creates the weakest ones. The  $\beta$ -drift principle (Fiorino and Elsberry, 1989) tells us when high tangential winds appear in the outer rainbands, typhoon has a strong cyclonic rotation and a dominant  $\beta$ -drift effect, so the TC track tends to experience a counterclockwise deflection. In this paper, NEVP has the largest tangential winds in the outer rainbands, so the typhoon track in NEVP deflects counterclockwise from that in CTRL (note that the influence of wind strength in the inner core is little

yet). In contrast, HLF\_AG has the smallest tangential winds, and hence the typhoon track in this experiment deflects clockwise from CTRL. On the whole, this study reveals that the variation of typhoon intensity can impact on its track.

Figure 3 gives the evolution of the typhoon's moving speed from various experiments. It is found that the moving speed in all experiments generally approximates the reality although the trend of the simulated typhoon traveling speed is contrary to the observation during 9–12 and 27–30 h. The observed 36-h-averaged traveling speed amounts to  $21.26 \text{ km h}^{-1}$  before the landfall of the true TC, but all the simulated typhoons travel faster than the observation. For instance, CTRL

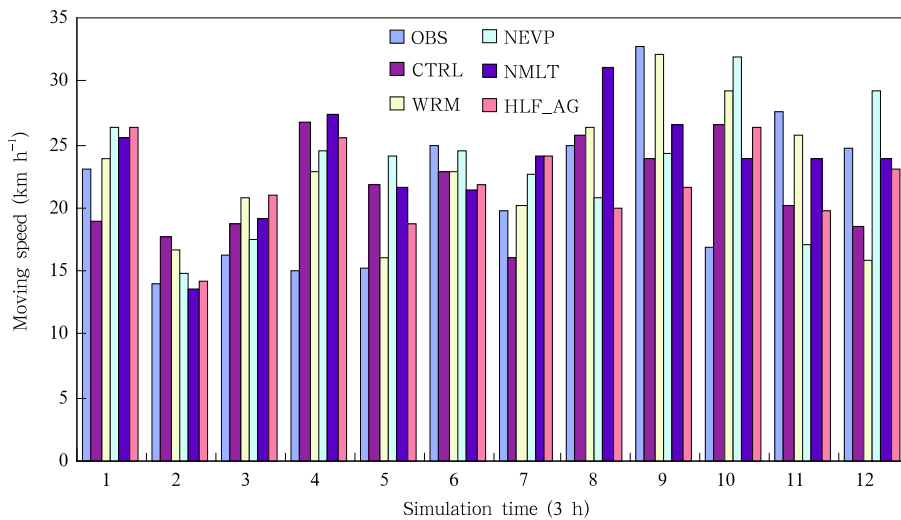


**Fig. 3.** The time series of observed and simulated moving speeds ( $\text{km h}^{-1}$ ) of Typhoon Rananim.

shows the smallest bias of  $0.23 \text{ km h}^{-1}$  relative to the observation, but NMLT has the biggest one of  $2.24 \text{ km h}^{-1}$ . In addition, it is known that although NEVP has the largest departure (about 200 km) in the final TC location from the observation, the traveling speed is not the fastest. Consequently, we can say that a reasonable cloud microphysical parameterization is of importance for the correct prediction of the typhoon's movement.

### 3. Impact of outer spiral rainbands on the typhoon intensity

From the above comparison analysis of the typhoon strength, we can see that the deepening and maintenance of Ranim can be captured by various experimental schemes during the early 24 hours.

However, all the experiments have a large reduction in typhoon intensity after 24 h. In this section, we will discuss the influence of outer spiral rainbands and environmental wind shear on the simulated typhoon strength near its landfall based on the CTRL results.

#### 3.1 Characteristics of the model cloud bands

The infrared satellite image at 0300 UTC 12 August (Fig. 4a) shows that the highly developed convective cloud system is present in the shoreward part of the typhoon-affected area, and the main body of cloud shrinks towards the TC center so that the convection intensity in the outer spiral rainbands is reduced as Ranim moves rotationally towards the shore. From 0400 to 1200 UTC 12 August, the strong convection appears mainly in the eyewall region and there exists the weak convective system in the outer rainbands

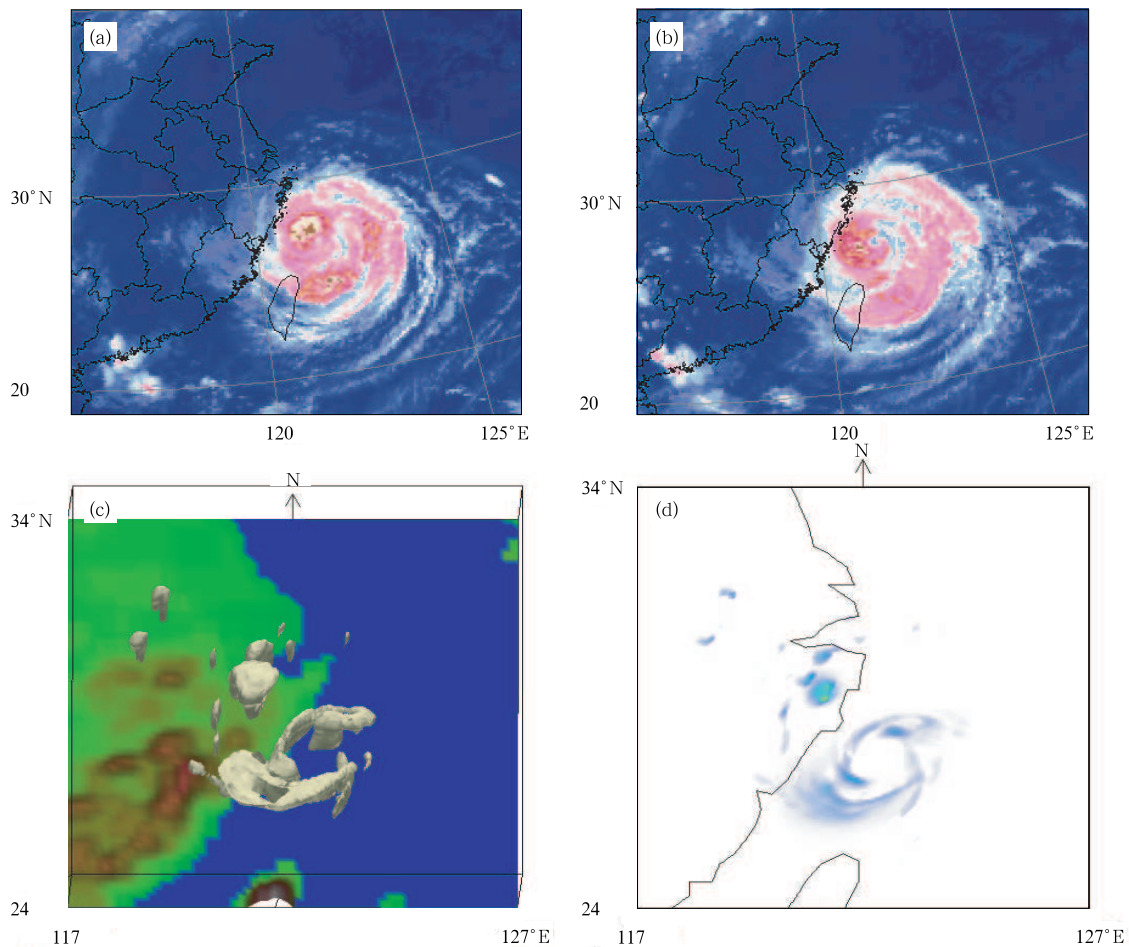


**Fig. 4.** Infrared satellite image at (a) 0300 UTC and (b) 0500 UTC 12 August 2004, and (c) simulation of  $2 \text{ g kg}^{-1}$  surface for total hydrometeors (in  $\text{kg kg}^{-1}$ ) and (d) three-dimensional structure of total hydrometeors (in  $\text{kg kg}^{-1}$ ) at 0500 UTC 12 August 2004.

(Fig. 4b).

Figures 4c and 4d describe the simulated three-dimensional distributions of the total content of hydrometeors. We can easily see that the model well depicts the cloud band distribution, though the convection in the shoreward part of spiral rainbands is much stronger than the reality. This convective cloud system in the shoreward quadrants is kept active till the landfall. It should be noted that the highly-developed outer rainbands can prohibit the maintenance and intensification of the eyewall convection, which will be demonstrated in detail in the next section.

Nevertheless, the simulated cloud system is weaker than the observation in the eastern quadrants of the typhoon, i.e., the outer rainbands contribute less to the strength of the cloud system during this period. This is because 1) the outer rainbands occur a bit far from the eyewall above the ocean, so cold and dry air parcels from the middle troposphere are warmed and moistened effectively through the upward transport of sea surface fluxes as they invade into the inner core region far from the eyewall, resulting in less strong influences of the outer rainbands; 2) the intensity (in terms of mosaic colors) comparison reveals that the convection in the outer rainbands is much weaker than that in the eyewall although there are widespread rainbands in the eastern part of the typhoon.

### 3.2 Influence of outer rainbands on the typhoon strength

Figure 5 gives the time-height cross-sections of azimuthally averaged radar reflectivity, vertical velocity, and pseudo-equivalent potential temperature beyond the eyewall. It can be seen that spiral rainbands are extremely weak during the first 10 hours. Then, rainbands develop gradually at lower and upper levels, indicating that snow and graupel are advected outwards from the eyewall in the upper troposphere and rain water concentration in the PBL is increased as well. Until 0000 UTC 12 August, the convection is absent or weak in the middle troposphere between 700 and 500 hPa. Hereafter, the convection in the outer rainbands experiences a rapid intensification and a strong convective tower appears. The radar echoes from the

convective clouds show that high reflectivity is present between 950 and 200 hPa with two peaks of the azimuthally averaged radar reflectivity in the PBL and 400 hPa respectively. Accordingly, intense updrafts occur simultaneously with the strong reflectivity. The azimuthally averaged vertical velocity has the peak value of above  $1 \text{ Pa s}^{-1}$  near 500 hPa. As a result, the intense convection in the outer rainbands forces the strong convergent flow in the lower troposphere outside the eyewall, which brings air parcels with high potential energy from the PBL to the middle and upper levels so that the pseudo-equivalent potential temperature there achieves high values at the same time. The convective activities in the spiral rainbands reduce PBL inflow towards the eyewall and prevent air parcels with high humidities and temperatures from advecting into the inner core. Therefore, the typhoon strength is suppressed, which agrees well with the results of Wang (2002).

The downdrafts associated with the spiral rainbands can also bring the cold and dry airflows into the PBL. When they are advected into the eyewall area, the temperature there will decline, which is a prohibitive factor to the typhoon strength. Furthermore, the evolution of pseudo-equivalent potential temperature indicates that low temperatures are dominant in the middle troposphere where the most marked variation of pseudo-equivalent potential temperature can be found. Figure 6 describes the radius-time cross-sections of thermodynamic fields at 950 hPa. Figure 6a shows that the stratiform precipitation tends to appear after 6 h in the rainbands  $3^\circ$  away from the TC center. Additionally, the cooling in the PBL due to the evaporation of rainfall tends to propagate radially towards the eyewall after 12 h (Fig. 6b). Consequently, cold and dry air parcels in the outer spiral rainbands are transported rotationally into the eyewall and then “erode” the inner core, so finally the typhoon intensity is reduced.

To further understand the structure and effect of outer rainbands of a TC, we carry out the dynamic, thermodynamic, and kinematic analyses using the model results for the period when the simulated typhoon is experiencing its weakening. It can be seen

from Fig. 7a that the model echo reflectivity in the outer spiral rainbands is stronger at the weakening stage of the typhoon (e.g., at 30 h) than that at its deepening and maintenance stage (e.g., at 24 h) with a big difference of 10 dBZ between them. At the weakening stage (Fig. 7b), the large range of low  $\theta_{se}$  below  $80^{\circ}\text{C}$  exists between 800 and 400 hPa about 200 km away from the TC center, although the temperatures

are somewhat higher than those at the deepening stage. In addition, in the spiral rainbands appear weak divergence (Fig. 7c) and clear subsidence (Fig. 7d). Although these downdrafts are of weak strength with the peak value of about  $0.1 \text{ Pa s}^{-1}$ , they can still transport the dry and cold air parcels downwards into the PBL. Then, the parcels are advected into the eyewall by the cyclonic inflow

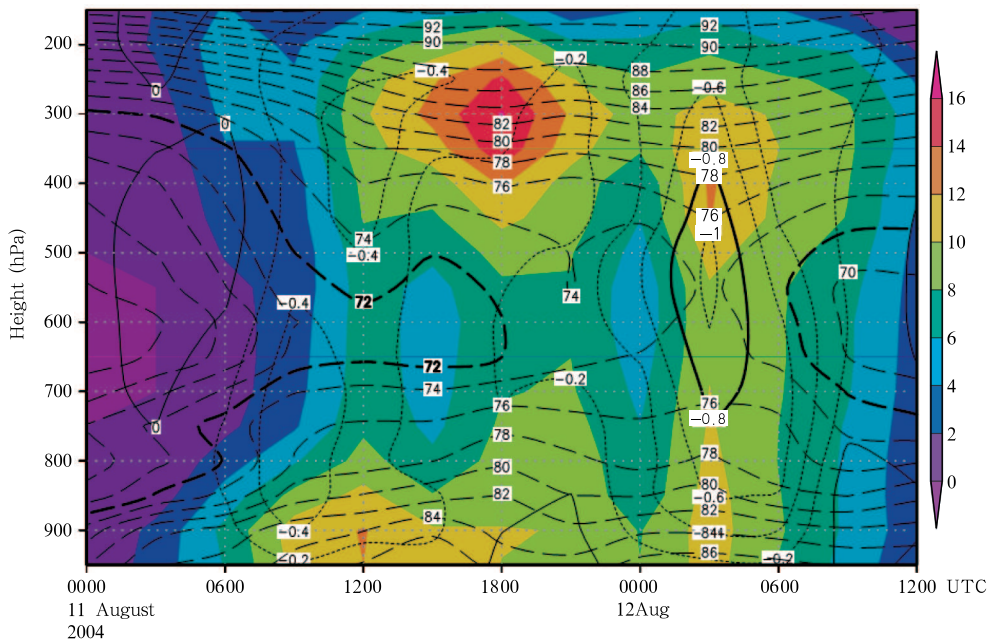


**Fig. 5.** The time-height cross-section of azimuthally averaged radar reflectivity (shaded; dBZ), vertical velocity (dotted line;  $\text{Pa s}^{-1}$ ), and pseudo-equivalent potential temperature (dashed line;  $^{\circ}\text{C}$ ), averaged from the radius of 275 to 325 km. The solid lines represent vertical velocity at the values of 0 and  $-0.8 \text{ Pa s}^{-1}$ .

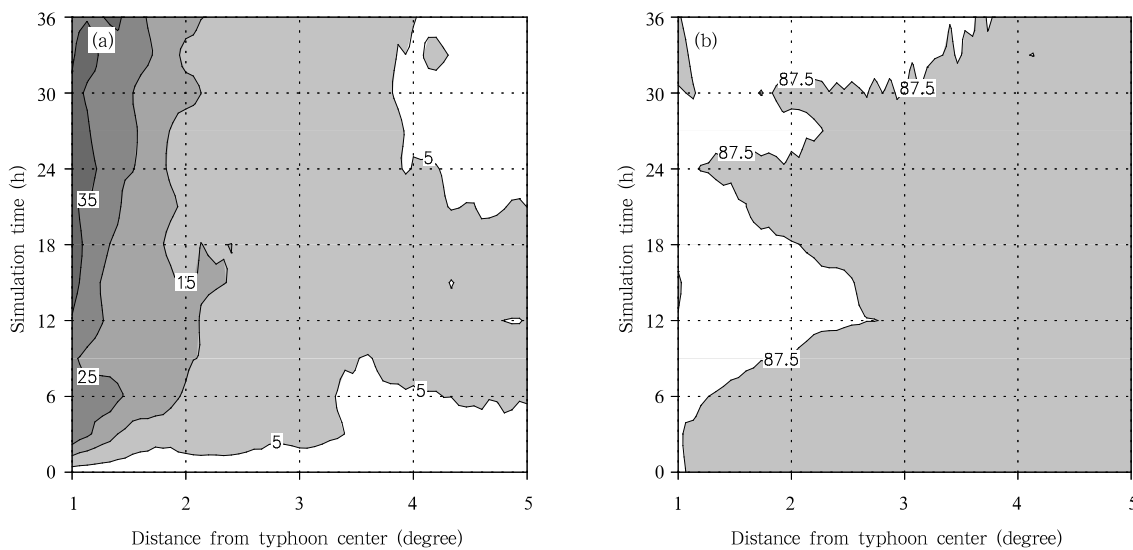


**Fig. 6.** The radius-time cross-sections at 950 hPa for (a) simulated radar reflectivity (dBZ) and (b) pseudo-equivalent potential temperature ( $^{\circ}\text{C}$ ).

(Figs. 7e and 7f). The heating from the ocean surface is unable to warm those dry and cold air parcels effectively since they are close to the eyewall, so the cold and dry descendent flow impacts markedly on the typhoon strength at the weakening stage. However, during the deepening stage of the typhoon, the even drier and colder air parcels are present at the middle levels in the outer rainbands, but they are almost never advected into the PBL and neither into the inner core since weak updrafts are always dominant there, thus

the typhoon intensity is well maintained.

Figure 8 is the radius-height cross-sections of hydrometeors at 30 h. Clearly, the model mixing ratios of various hydrometeors 200 km away from the typhoon center at the weakening stage are larger than those at the deepening and maintenance stage. Therefore, higher reflectivity of the model radar echo can be found in the outer rainbands at this time. The mixing ratios of cloud water, rain water, cloud ice, snow, and graupel reach their peak values of 0.05, 0.2, 0.15,

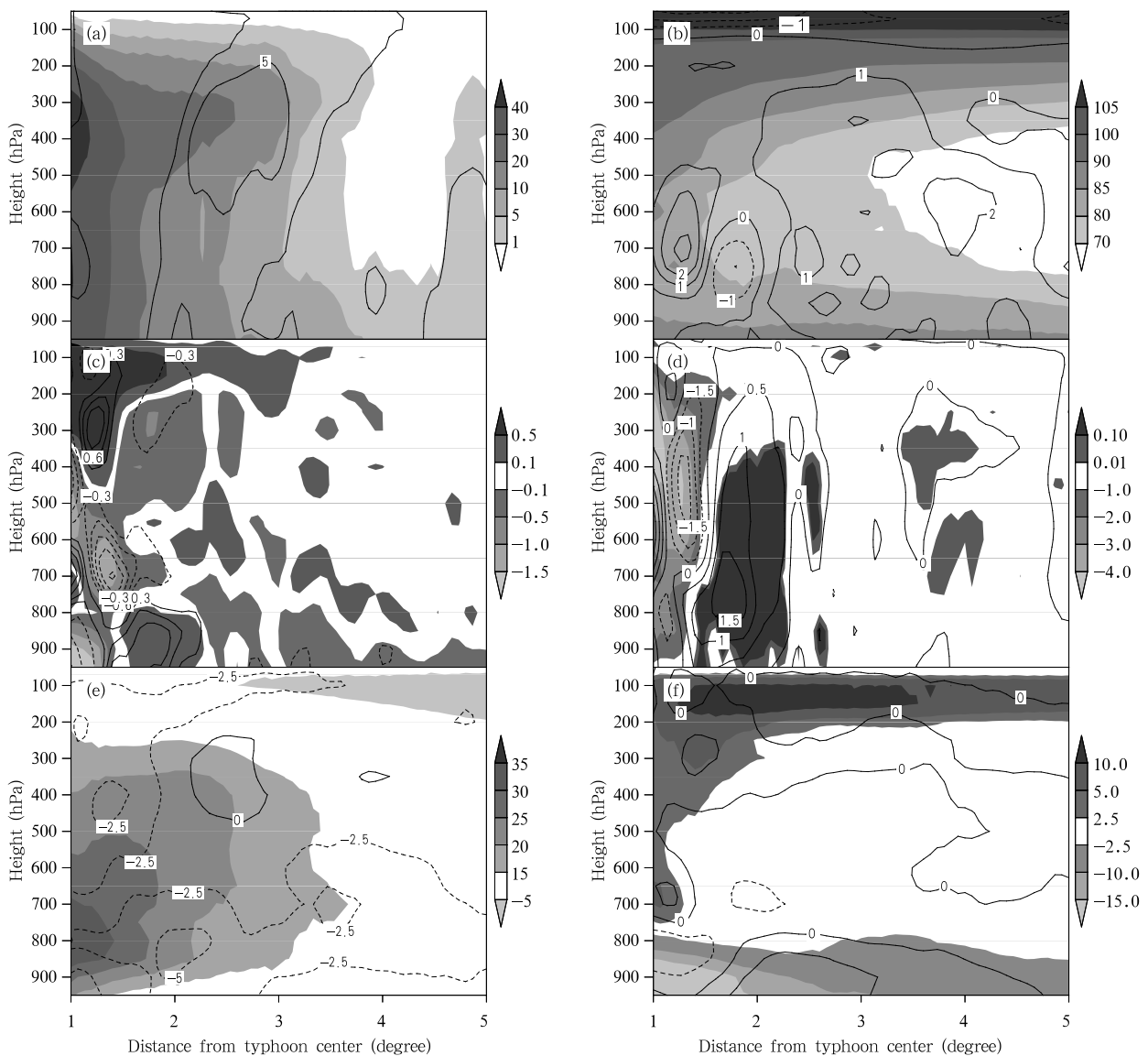


**Fig. 7.** The radius-height cross-sections (shaded) for (a) radar reflectivity (dBZ), (b) pseudo-equivalent potential temperature ( $^{\circ}\text{C}$ ), (c) divergence ( $10^{-4} \text{ s}^{-1}$ ), (d) vertical velocity ( $\text{Pa s}^{-1}$ ), (e) tangential wind speed ( $\text{m s}^{-1}$ ), and (f) radial wind speed ( $\text{m s}^{-1}$ ) at 30-h integration time, superposed by their respective differences (contoured) between 24 and 30 h.

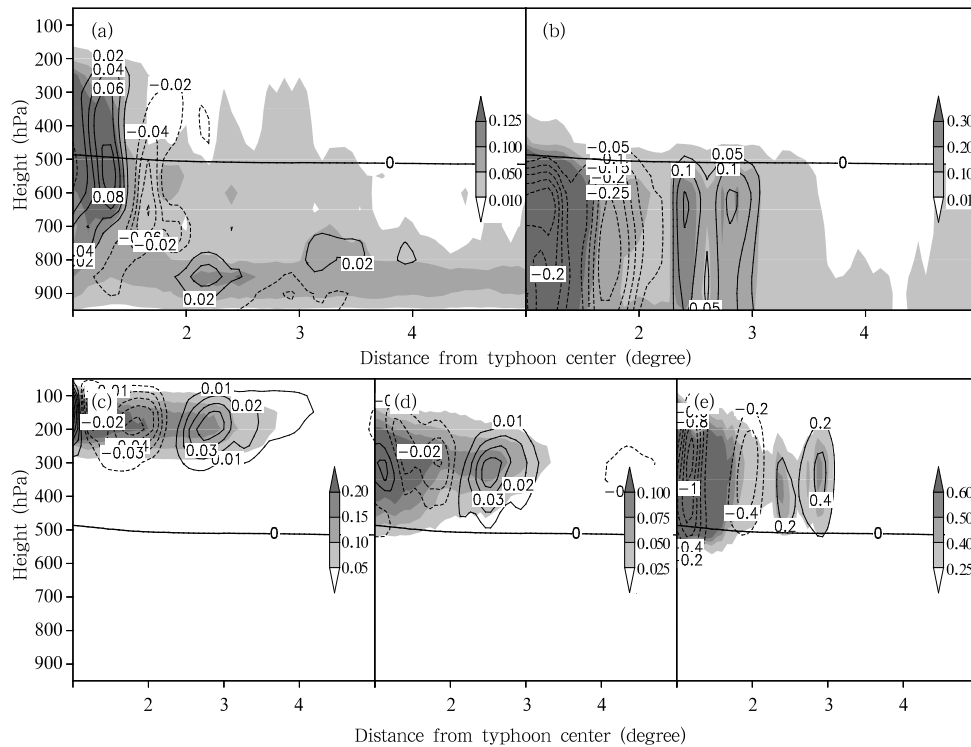


**Fig. 8.** The radius-height cross-sections of mixing ratio (shaded;  $\text{g kg}^{-1}$ ) for (a) cloud water, (b) rain water, (c) cloud ice, (d) snow, and (e) graupel at 30-h integration time, superposed by their respective differences (contoured;  $\text{g kg}^{-1}$ ) between 24 and 30 h.

0.075, and  $0.4 \text{ g kg}^{-1}$ , respectively, and they have the content increment of 0.04, 0.15, 0.04, 0.04, and  $0.4 \text{ g kg}^{-1}$  compared with those in the mature stage of the typhoon. The cooling due to the sublimation of cloud ice detrained from the stratiform cloud and due to the melting of snow and graupel below the freezing level, and the evaporative cooling effect of cloud water and rain water can all result in or strengthen the downdrafts in the spiral rainbands. Then, the subsidence flow can bring the cold and dry air parcels from the middle and upper levels to the PBL. Moreover, the evaporation of rain drops themselves can cool the air and decrease the temperature around them. As a result, the cold and dry flow will “erode” the eyewall and then reduce the strength of typhoon when they are advected into the inner core.

#### 4. Environmental effects on the typhoon intensity

The weakening of the simulated typhoon near its landfall can be explained as well through analyzing

background environmental effects. From the time-height cross-sections of the environmental flow of the typhoon (Fig. 9), we can see that the model vertical wind shear is generally similar to that in the NCEP analysis although the model wind shear is stronger. During the early 24 hours, the vertical wind shear is weak for both the simulation and the observation with southeasterly flows at all levels. After 0000 UTC 12 August, the southwesterly flow is gradually dominant at lower levels whereas the southeasterly is still present at upper levels, which result in strong vertical wind shear. At 0600 UTC 12 August, for example, the latitudinal and longitudinal wind differences between 200 and 850 hPa amount to  $-5.776$  and  $-1.835 \text{ m s}^{-1}$  for the NCEP analysis; whereas for the simulation, they reach  $-7.902$  and  $-4.362 \text{ m s}^{-1}$ , respectively. It is well known that strong vertical wind shear is unfavorable for the maintenance of typhoon strength. The analysis in this paper agrees well with this common sense: the NCEP analysis-based maximum surface wind speed has a slight drop of  $1 \text{ m s}^{-1}$  between 0600 and 1200 UTC since its vertical wind shear is small, whereas the

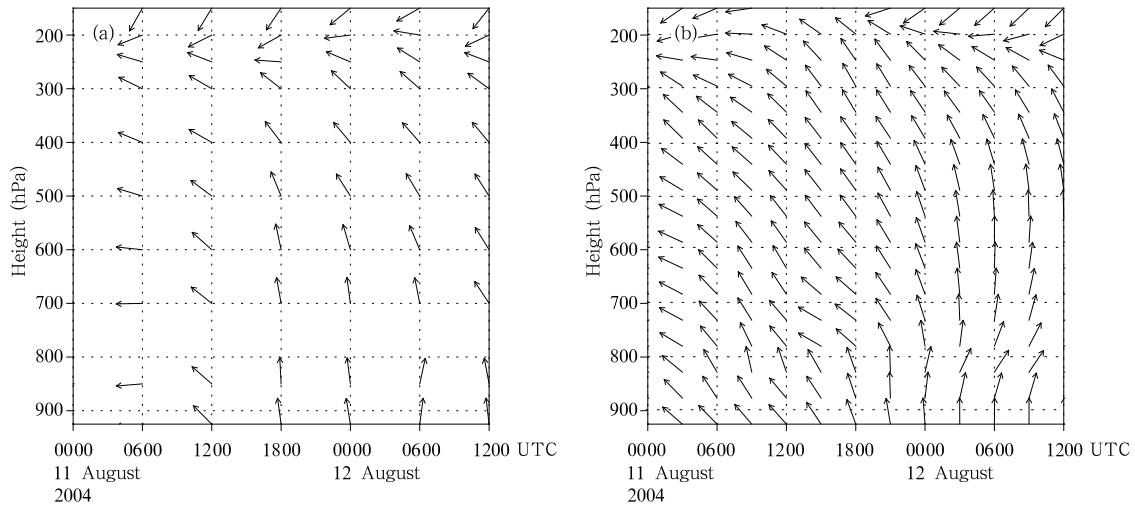


**Fig. 9.** The time-height cross-sections of the environmental flow ( $\text{m s}^{-1}$ ) of Typhoon Rananim. (a) NCEP analysis and (b) simulation.

model has a large vertical wind shear so the maximum surface wind speed drops dominantly with a decrease of  $10 \text{ m s}^{-1}$  during that stage. In a word, the strong model vertical wind shear can partly lead to the reduction of the simulated typhoon intensity.

In addition, the SST is also an important factor for the maintenance of the typhoon strength. We can see from the daily averaged model SST (figure omitted) that Typhoon Rananim travels mainly along the SST isotherm. As a result, a sharp reduction in the model intensity of typhoon is not brought about by the SST forcing.

## 5. Summary

The impact of cloud microphysical processes on the intensity and track of Typhoon Rananim is studied through numerical sensitivity analysis. The reason why the simulated typhoon weakens near its landfall is further studied in this part of the paper, with the influences of microphysical processes and environmental wind shear being focused on.

It is found that the microphysics can affect the intensity and track of the typhoon to a great extent. The final maximum surface wind speed is the closest to the truth, about  $7 \text{ m s}^{-1}$  greater than that of all other experiments when the cooling effect due to the evaporation of rain water is excluded; however,

the typhoon's landfall location has the biggest bias of about 150 km away from the observation. Additionally, the simulated typhoon has the fastest traveling speed, about  $2.24 \text{ km h}^{-1}$  faster than that of the reality with the exclusion of the melting of snow and graupel.

The cloud microphysical processes can strengthen and even create the outer spiral rainbands, which can then increase the local convergence beyond the TC center and prevent more moisture and energy from advection into the inner core of the typhoon. Also, the well-developed outer rainbands are supposed to bring dry and cold air masses from the middle troposphere to the PBL. Moreover, the other branch of the cold airflow originates from the evaporation of rain water in the PBL while it is falling. When these cold and dry air parcels are transported by strong inflows to the typhoon inner core, the eyewall will suffer "cold invasion", which results in the intensity reduction of the modeled typhoon.

In addition, the increment of the model environmental vertical wind shear is another factor that may lead to the weakening of the simulated typhoon near its landfall.

The warm cloud microphysics brings about a faster intensification of a typhoon, but the final intensity is close to that of the ice-phase process. This result is similar to the idealized TC experimental

analysis of Wang (2002), but different from the conclusion by Kong et al. (1991). Therefore, it is inferred that the cloud microphysics influencing Typhoon Rananim may notably differ from that affecting severe thunderstorms.

It is known that the simulation and prediction of typhoon intensity is still one of the arduous jobs in typhoon studies. Also, it seems to be difficult currently for us to simulate accurately the deepening and maintenance of Typhoon Rananim near its landing. For instance, the Japan mesoscale reanalysis-based surface maximum wind speed is  $10 \text{ m s}^{-1}$  less than the observation, and its central sea level pressure is 20 hPa weaker than the reality at the Rananim's landfall.

**Acknowledgments.** The authors are grateful to Prof. Zhou Xiaoping at IAP/CAS, Prof. Yuqing Wang at Hawaii University, Prof. Xu Huanbin at Beijing Institute of Applied Meteorology, Prof. Zhou Tianjun at LASG/IAP/CAS, and Prof. Guosheng Liu at FSU for their advice on the typhoon simulation. We also thank Mrs. Sun Jiao at Beijing Institute of Applied Meteorology for the English polishing.

## REFERENCES

- Barnes, G. M., E. J. Zipser, D. Jorgensen, and F. Marks Jr., 1983: Mesoscale and convective structure of a hurricane rainband. *J. Atmos. Sci.*, **40**, 2125–2137.
- Chen, L. S., H. B. Luo, Y. H. Duan, and H. Yu, 2004: An overview of tropical cyclone and tropical meteorology research progress. *Adv. Atmos. Sci.*, **21**, 505–514.
- Fiorino, Michael, and Russell L. Elsberry, 1989: Some aspects of vortex structure related to tropical cyclone motion. *J. Atmos. Sci.*, **46**, 975–990.
- Kong Fanyou, Huang Meiyuan, and Xu Huaying, 1991: 3D numerical simulation studies on the effect of ice microphysics on the cumulus development. *Sci. China (Series B)*, **21**(9), 1000–1008.
- Li Ying, Chen Lianshou, and Wang Jizhi, 2004: The diagnostic analysis on the characteristics of large scale circulation corresponding to the sustaining and decaying of tropical cyclone after its landfall. *Acta Meteor. Sinica*, **62**, 167–179. (in Chinese)
- Pattnaik, S., and T. N. Krishnamurti, 2007: Impact of cloud microphysical processes on hurricane intensity. Part II: Sensitivity experiments. *Meteor. Atmos. Phys.*, **97**, 647–662.
- Powell, M. D., 1990: Boundary-layer structure and dynamics in outer hurricane rainbands. Part II: Down-draft modification and mixed layer recovery. *Mon. Wea. Rev.*, **118**, 918–938.
- Wang Yuqing, 2002: An explicit simulation of tropical cyclones with a triply nested movable mesh primitive equation model: TCM3. Part II: Model refinements and sensitivity to cloud microphysics parameterization. *Mon. Wea. Rev.*, **130**, 3022–3036.
- Zhu Tong and Da-Lin Zhang, 2006: Numerical simulation of Hurricane Bonnie (1998). Part II: Sensitivity to varying cloud microphysical processes. *J. Atmos. Sci.*, **63**, 109–126.